

Topological characteristics of plane sections of polycrystals

Gregory S. Rohrer*, Herbert M. Miller¹

*Department of Materials Science and Engineering, Carnegie Mellon University,
Pittsburgh, PA 15213-3890, USA*

Received 8 February 2010; received in revised form 15 March 2010; accepted 17 March 2010
Available online 8 April 2010

Abstract

Homology metrics have been used to assess the connectivity of grain boundary networks in plane sections of polycrystals. The analysis is based on orientation maps, and four characteristic microstructure types were examined: SrTiO₃ microstructures with normal and bimodal grain size distributions and two Ni microstructures with different concentrations of $\Sigma 3$ grain boundaries. The inverse connectivity, defined as the ratio of the number of independent pieces of the network to the number of closed loops, is proposed as a metric for the extent to which certain types of grain boundaries are connected. The variation in inverse connectivity with disorientation threshold, below which boundaries are excluded from the network, produces distinct signatures for the different microstructures.

© 2010 Acta Materialia Inc. Published by Elsevier Ltd. All rights reserved.

Keywords: Topology; Microstructure; Grain boundaries; Grain boundary junctions; Twin grain boundaries

1. Introduction

Certain properties of polycrystals, for example corrosion resistance, are influenced by the mesoscale structure of the grain boundary network [1–4]. In the present context “mesoscale” refers to structural features that are larger than the atomic scale but relatively small in comparison with the material’s external boundaries. For a single phase polycrystal the two main characteristics of the mesoscale structure are the relative areas of the different types of grain boundaries within the microstructure and the way that they are connected.

The vast majority of prior work characterizing polycrystals has focused on measuring the relative areas of the different types of grain boundaries [1–8]. For such studies different types of grain boundaries have been discriminated based on whether or not they are deemed to be special (a binary classification) [3], based on their lattice disorienta-

tion (this can be a single disorientation angle or a three parameter description of the transformation that brings the two lattices into coincidence) [2] or based on all five crystallographic characteristics of the boundary (the disorientation and the grain boundary plane orientation) [5–8]. The method for discriminating different boundary types is selected based on the problem at hand. For example, in cubic close-packed structures twins and twin related boundaries are thought to have enhanced corrosion resistance with respect to other boundaries and are labeled special, while the rest are not, so the binary classification is most frequently used [4,9].

Fewer studies have attempted to correlate the connectivity of grain boundaries in the microstructure with the properties. The most frequently used approach has been to classify the types of triple junctions present within the microstructure [10–15]. In this case junctions are usually classified according to the number of special boundaries in the triplet. Others have evaluated the sizes of twin related clusters, which typically exceed the mean grain size [16–18]. The connectivity of networks of special grain boundaries has also been studied using percolation metrics [19]. Based on an analysis of percolating clusters, Schuh

* Corresponding author. Tel.: +1 412 268 2696; fax: +1 412 286 3113.
E-mail address: gr20@andrew.cmu.edu (G.S. Rohrer).

¹ Present address: Integran USA, 2580 Smallman Street, Pittsburgh, PA 15222, USA

et al. [19] found that the special boundary fraction is not a reliable indicator of network topology.

The mathematical tools of topology have been applied to materials research for many years, but there are still relatively few examples [20–27]. A 1972 review by Steele [20] covered a number of applications to single and multiphase materials. More recent work has concentrated on using topology to characterize multiphase systems [21–26]. However, a recent paper by Wanner et al. [27] took a new approach and explored the topology of the mechanical response fields in simulated polycrystals. As part of this study the authors used homology metrics to characterize the connectivity of grain boundaries in a simulated polycrystal with uniaxial symmetry. The requirement for such an analysis, not used in any of the previous studies, is a knowledge of crystal orientations. The present research was undertaken with the goal of using a similar approach to characterize real materials and to evaluate the connectivity of boundaries in plane sections of cubic materials with four prototypical microstructures. In particular, the topology of materials with a normal grain size distribution, a bimodal grain size distribution and different concentrations of $\Sigma 3$ grain boundaries are analyzed and compared.

Based on the findings presented here, it is proposed that homology metrics are sensitive indicators of the grain boundary network structure. In two dimensions these topological parameters measure the number of independent pieces of the network (referred to as B_0) and the number of closed loops (referred to as B_1) [27]. In the context of plane sections of grain boundary networks B_0 measures groups of grain boundaries not connected to the rest of the network and B_1 measures continuous, closed paths of grain boundaries. Based on the present results, the ratio of B_0 – B_1 , referred to here as β_{01} or the inverse connectivity, is proposed as a metric for network connectivity. The ratio varies with the subset of boundaries considered and the variation in β_{01} as a function of the disorientation angle threshold is a characteristic of the type of microstructure, providing information beyond that available from relative area measurements.

2. Methods

2.1. Specimens

Micrographs of four specimens were examined in this study. The first was SrTiO₃ with a bimodal grain size distribution. The second was SrTiO₃ with a normal (unimodal) grain size distribution. The third and fourth samples were both commercial purity Ni, but in one 42% of all boundary length was $\Sigma 3$ type boundaries (referred to as low $\Sigma 3$) and in the other 63% of all boundary length was $\Sigma 3$ type boundaries (referred to as high $\Sigma 3$). Note that $\Sigma 3$ is the designation assigned to grain boundaries with a disorientation of 60° around [1 1 1]. Orientation maps of the four samples are illustrated in Fig. 1.

The SrTiO₃ sample was produced from Aldrich SrTiO₃ (<5 μm , 99% pure) powder, which was dry ground and uniaxially compacted to form a cylindrical pellet. The sample was then heated in air to 900 °C for 10 h, then to 1340 °C for 10 h and, finally, to 1470 °C and, after reaching this temperature, it was immediately cooled in the furnace. This treatment produced the first sample with the bimodal grain size distribution, referred to as BMGSD. After recording orientation maps the sample was annealed for 3 h at 1470 °C in air. This treatment produced the second sample with the unimodal grain size distribution, referred to as NGSD. To prepare the surfaces the samples were lapped flat using a Logitech PM5 with a flat cast iron plate and 3 μm alumina slurry. They were then polished using 0.02 μm colloidal silica (Buehler Mastermet II) for approximately 30 min. Next came a brief, relatively low temperature anneal at 1100 °C for 1 h in air to heal residual damage. A thin carbon coating was then evaporated onto the sample to eliminate charging effects in scanning electron microscopy (SPI-Module Carbon Coater).

The Ni samples were obtained from Integran Technologies Inc. The samples were derived from the same source, but were described by the manufacturer as “reference” and “grain boundary engineered”. The samples had distinct microstructures and the grain boundary character distributions have been described in detail elsewhere [6,28]. The key features of these microstructures, for the present study, were that they had the same grain size but different relative areas of $\Sigma 3$ grain boundaries. Specifically, both had a grain size of 40 μm and the measured grain boundary lengths per area differed by only 3% [28]. The sample with a smaller length fraction of $\Sigma 3$ boundaries will be referred to as low $\Sigma 3$ and the one with the larger length fraction will be referred to as the high $\Sigma 3$ sample. The surfaces were prepared for electron backscatter diffraction (EBSD) mapping by grinding with SiC and diamond abrasives, followed by a vibratory chemo-mechanical process with 0.05 μm SiO₂ slurry and, finally, electropolishing in a chilled 9:1 methanol:perchloric acid solution.

2.2. Electron backscatter diffraction measurements

Orientation maps of the SrTiO₃ samples were recorded with a 60° sample tilt and a 25 kV beam in a Phillips XL40 FEGSEM using TSL/OIM software v. 4.5 (TSL/EDAX). For the BMGSD sample we considered a 174 × 105 μm area that was mapped with a 0.35 μm step size between orientation points. For the NGSD sample we considered a 1.5 × 1.6 mm area mapped with a 2 μm step size. The orientation data were then processed to remove spurious observations. Processing included a grain dilation in which pixels not belonging to grains of a defined minimum size were logically reassigned to accepted grains and orientation averaging, which assigns a single average orientation to each pixel in a grain. The minimum misorientation defining a boundary was defined to be 5°. A pseudosymmetry correction was also employed

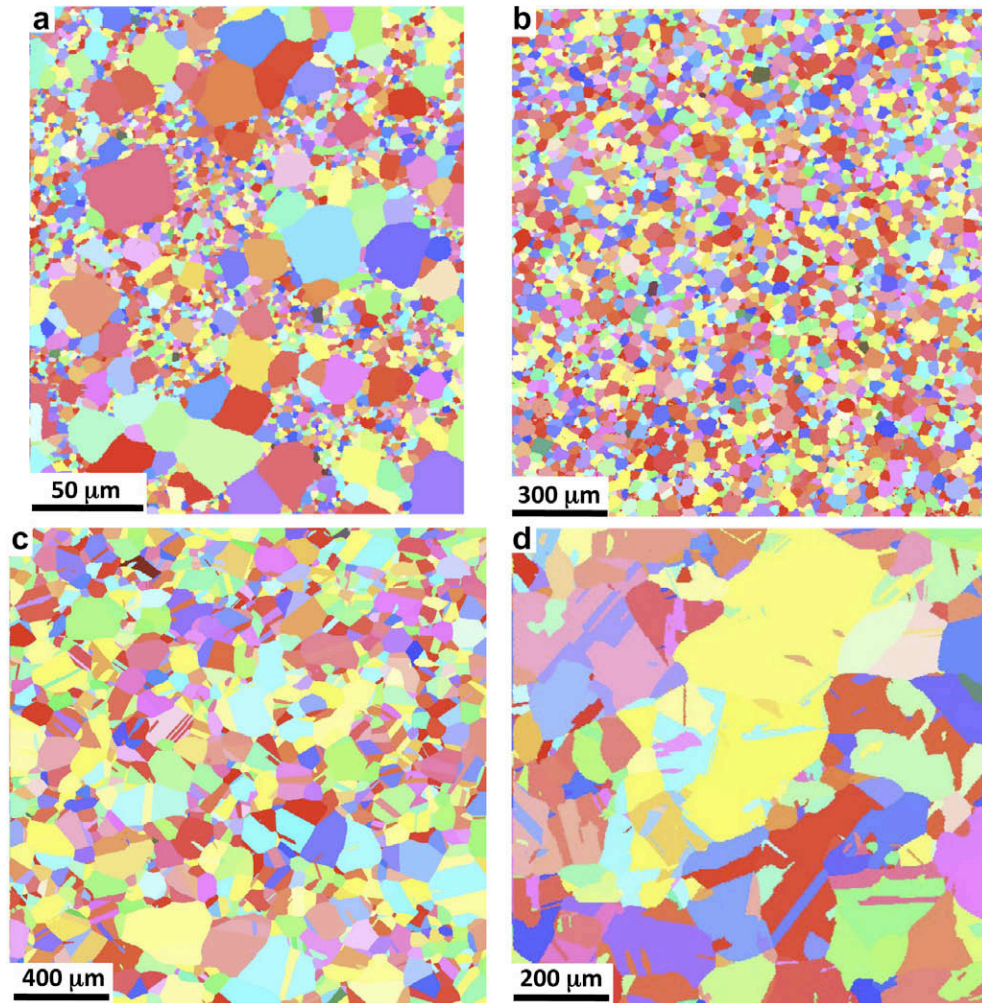


Fig. 1. Inverse pole figure maps of the four characteristic microstructures. (a) SrTiO₃ with a bimodal grain size distribution, (b) SrTiO₃ with a normal grain size distribution, (c) Ni with 42% Σ₃, by length, and (d) Ni with 63% Σ₃, by length.

to correct for a specific misindexing problem involving difficult to distinguish orientations (45° rotation around [0 0 1]). The average grain size of the BMGSD sample was 2.89 μm and the average grain size NGSD sample was 23.2 μm.

Orientations maps for the Ni were obtained similarly, except that a 20 kV beam was used. As described above, the orientation data were processed to remove spurious observations using a “grain dilation clean-up” in the OIM software. A single orientation was then assigned to each grain by averaging all of the orientations belonging to a single grain.

2.3. Image processing

The orientation maps for both Ni and the SrTiO₃ consist of discrete orientations, specified by three Euler angles, arranged in a hexagonal pattern. However, the computational homology tools used here operate on images comprising only black and white pixels arranged in a square lattice pattern. So, the first step in processing the images

was to resample the maps onto a square lattice. Next, for each pixel the disorientation was calculated between the pixel of interest and the eight nearest neighbor pixels. The disorientation angle was the minimum misorientation angle among all symmetrically indistinguishable misorientations. From the eight disorientations the one with the maximum angle was selected and assigned to that pixel. When this was repeated for every pixel in the map the result was a disorientation map. Note that while the selection was made on the basis of the disorientation angle, the complete disorientation was parameterized by three Euler angles and these were preserved in the disorientation map. In such a map the disorientation angle is zero within the grains because all of the neighbors have the same orientation, but it has values greater than zero at the grain boundaries. For cubic crystals disorientation angles can vary between 0° and 62° [29]. Therefore, if a gray level between 0 and 255 is assigned to each pixel, proportional to the disorientation angle, an image is produced in which the darker points indicate the positions of grain boundaries. Examples of these images are illustrated in Fig. 2.

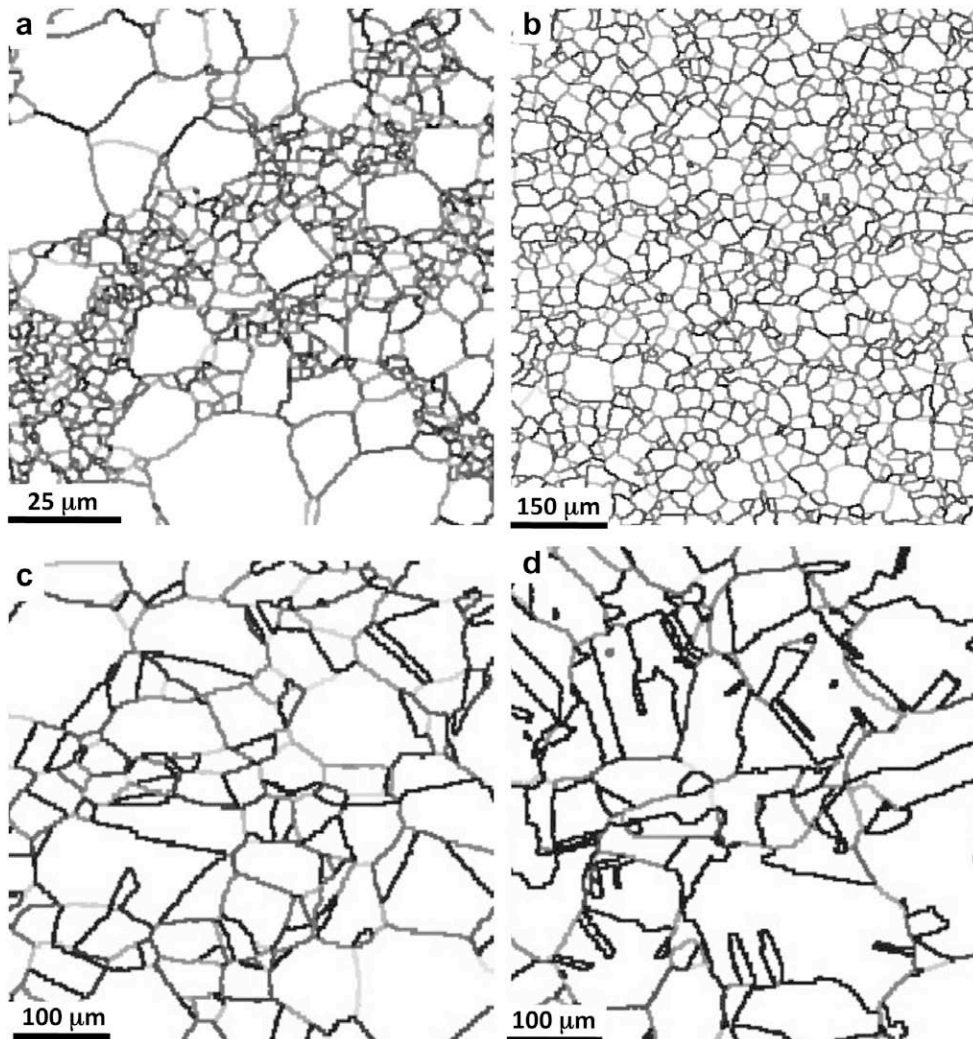


Fig. 2. Disorientation maps of the four microstructures. The boundaries are shaded according to disorientation, with white corresponding to 0° disorientation and black to 62° . Each image is an enlarged subset of one of the maps in Fig. 1, to emphasize the details of the network. (a) bimodal SrTiO_3 , (b) unimodal SrTiO_3 , (c) low $\Sigma 3$ Ni, (d) high $\Sigma 3$ Ni.

2.4. Calculation of homology metrics

Homology metrics were calculated with the software CHomP, which is available without cost [30,31]. The only processing step to prepare the disorientation map for analysis by CHomP was a thresholding operation that made all of the pixels either black or white. The simplest way to do this was to color all pixels with a disorientation angle greater than zero black and all pixels with a disorientation angle equal to zero white. Maps were also created based upon subsets of boundaries selected by their disorientation. For the Ni sample one set was created by grouping together all those grain boundaries within Brandon's criterion [32] of the $\Sigma 3$, $\Sigma 9$ and $\Sigma 27$ disorientations (we will refer to these as $\Sigma 3^n$ boundaries) and a complementary set was created from the remaining boundaries. The other partitioning method used here was to create complementary subsets of all boundaries less than or greater than a certain disorientation angle. From the processed maps

the program CHomP returns B_0 and B_1 , known in the topology literature as Betti numbers [27]. These values are integers, but their ratio, β_{01} , is taken to be a real number which is not defined under the condition that $B_1 = 0$. Note that β_{01} should be scale invariant, as long as the plane section contains enough grains. This makes it possible to compare maps from different areas and materials with different grain sizes. This assumption is examined below.

3. Results

The boundary map for the SrTiO_3 sample with the bimodal grain size distribution is illustrated in Fig. 3. As noted in the introduction, B_1 is the number of closed loops, which is also the number of complete grains in the image ($B_1 = 2486$), and B_0 is the number of disconnected segments ($B_0 = 4$). For a complete, ideal grain boundary network $B_0 = 1$. The most reasonable microstructural explanation for values of B_0 in excess of one are so-called island grains,

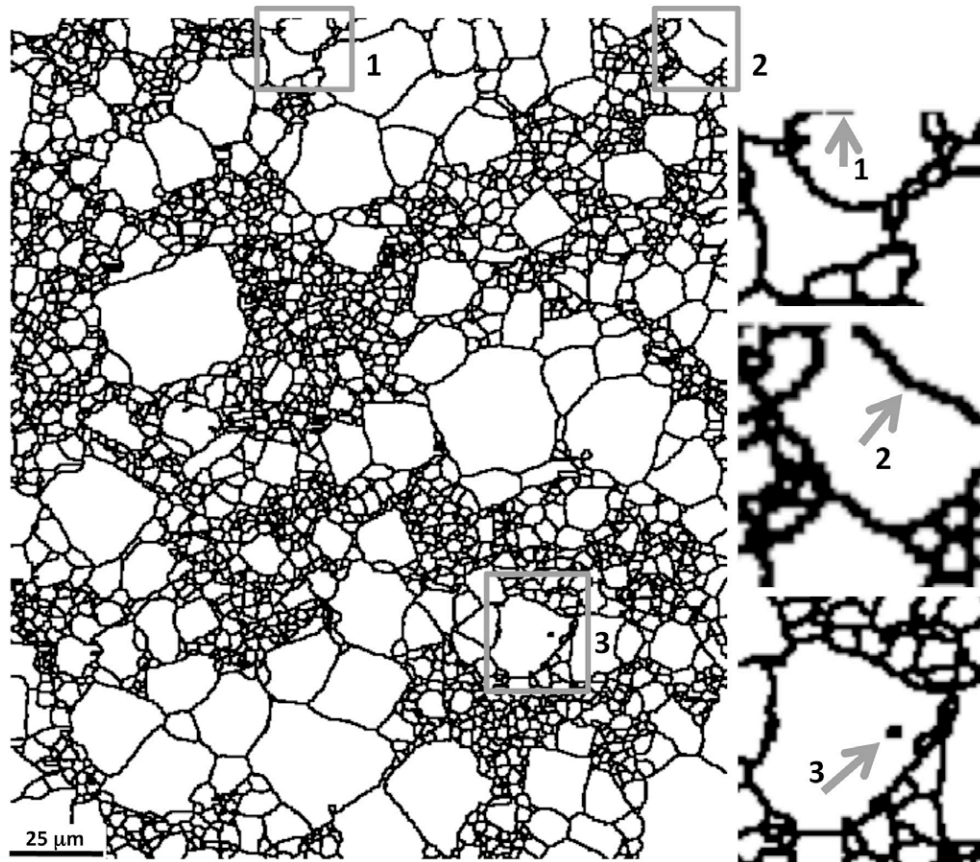


Fig. 3. Thresholded grain boundary map for the bimodal SrTiO₃. The three insets show details that create disconnected pieces of the network and increase B_0 above one. (1) A tangential boundary on the edge, (2) a boundary crossing a corner of the image, (3) an island grain.

where a closed loop grain boundary occurs completely within another grain on the plane section. The second, more trivial, explanation for disconnected components are artifacts associated with the edges of the images. Boundaries that cross a corner of the image within a white region, boundaries that tangentially intersect an edge of a white region and groups of misindexed pixels within grains that are not eliminated during the clean-up procedure can all increase the number of disconnected components. For

example, for the microstructure in Fig. 3 the four independent objects are the main part of the grain boundary network, a tangential boundary (inset 1), a corner crossing segment (see inset 2) and an island grain (see inset 3). Therefore, two of the four are artifacts.

The boundary maps for the other three structures are shown in Fig. 4 and the homology metrics for all of the samples are summarized in Table 1. Note that for the ideal case $\beta_{01} = 1/N$, where N is the number of grains. In fact,

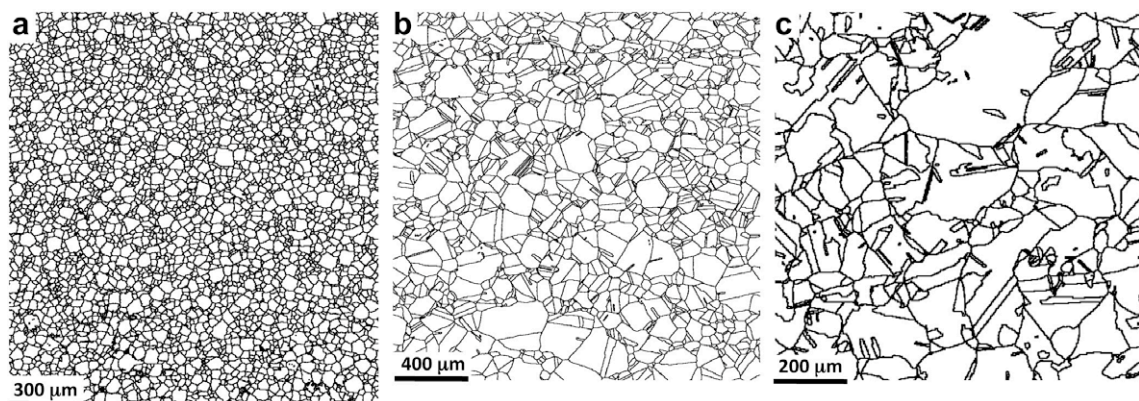


Fig. 4. Thresholded grain boundary maps for three samples. (a) Unimodal SrTiO₃, (b) low $\Sigma 3$ Ni, (c) high $\Sigma 3$ Ni.

Table 1
Topological parameters of the four samples.

Sample		B_0	B_1	β_{01}
1	Bimodal grain size distribution	4	2486	0.002
2	Normal grain size distribution	11	3964	0.003
3	Low $\Sigma 3$	18	2053	0.009
	$\Sigma 3''$	792	254	3.1
4	Non- $\Sigma 3''$	47	391	0.12
	High $\Sigma 3$	30	484	0.062
	$\Sigma 3''$	118	223	0.53
	Non- $\Sigma 3''$	60	7	8.6

there will always be some contribution to β_{01} from both real island grains and edge artifacts. For sample 2, like sample 1, the disconnected components arose from a mixture of island grains and edge artifacts. Nevertheless, the inverse connectivity β_{01} remained a few parts per thousand. For the Ni microstructures β_{01} was larger. In the low $\Sigma 3$ microstructure (Fig. 4b) there were 18 disconnected components, which included 15 twinned island grains, one island on the edge of the image and one corner crossing artifact. In the high $\Sigma 3$ microstructure (Fig. 4c) there were 30 disconnected components, which included 22 twinned island grains, four islands at the periphery and three features that may have been edge artifacts or peripheral island grains. Therefore, even when artifacts were accounted for, the fraction of island grains was measurably larger in the twinned microstructure than in the non-twinned structures, and this resulted in a larger value of inverse connectivity. It should be pointed out that in three-dimensions it is likely that these island twins were actually fully connected with the microstructure. However, in plane sections this is a clear distinguishing characteristic of the twinned microstructure.

To test how representative these metrics are of the microstructure, B_0 and B_1 were calculated for four different areas of the same microstructure, the high $\Sigma 3$ sample. All of the input images had identical lateral dimensions (1×1 mm) and, because these images had fewer grains than the others, were expected to exhibit maximum variability. For these areas B_0 had a mean value of 31.2 and a standard deviation of 5.8. B_1 had a mean value of 498 and a standard deviation of 80.9. Therefore, the standard deviations were 16–18% of the mean values. The mean value of β_{01} was 0.064 and the standard deviation was 0.016. Even with this degree of uncertainty, the measured inverse connectivity of the high $\Sigma 3$ sample was quantitatively different from the other three.

In this analysis it is assumed that B_0 and B_1 are proportional to area in the same way and, therefore, β_{01} is independent of area, as long as the field of view contains enough grains. If this is so, then it is possible to compare results taken from regions with different areas. To test this idea progressively smaller areas were extracted from the same image (the low $\Sigma 3$ sample) consisting of 100%, 82%, 75%, 52%, 42% and 26% of the total area. The mean value of inverse connectivity measured from these areas was 0.009 and the standard deviation was 0.001. Furthermore,

the ratio did not show a monotonic dependence on the area fraction. The observed variations were dominated by small fluctuations in B_0 created by the edge effects discussed above. Therefore, it was concluded that if there are enough grains in the image β_{01} is constant with image size. In this study the smallest number of grains was 472. The lower limit for the number of grains at which edge effects begin to dominate the result was not determined.

Next, the Ni microstructures are reconsidered after separating the $\Sigma 3''$ and non- $\Sigma 3''$ boundaries, as illustrated in Fig. 5. The network of $\Sigma 3''$ boundaries in the low $\Sigma 3$ sample was clearly disconnected and this was reflected in a value of β_{01} greater than one. On the other hand, the network of non- $\Sigma 3''$ boundaries (Fig. 5b) was relatively connected and this was reflected in a value of β_{01} less than one and 26 times smaller than the ratio in the $\Sigma 3''$ network (see Table 1). The situation was reversed for the high $\Sigma 3$ sample. In this case β_{01} was <1 for the $\Sigma 3''$ boundaries (see Fig. 5c). The inverse connectivity of the network of non- $\Sigma 3''$ boundaries was 16 times larger, indicating that it was relatively disconnected compared with the network of $\Sigma 3''$ boundaries.

Fig. 6 shows the inverse connectivity (β_{01}) for all boundaries greater than a threshold disorientation angle as a function of the threshold angle. Obviously, the microstructure became less connected as boundaries were removed from the network and this caused β_{01} to increase continuously with disorientation angle. The slope was initially small, continuously increased to about 45° and then became smaller. This was mostly because of the misorientation distribution. The misorientation distribution for these samples was random and the distribution of boundaries was therefore a peaked function with a maximum at 45° [29]. Therefore, at low threshold angles relatively few boundaries are removed with successive increments in the disorientation angle, but this increases as the maximum is reached. After the maximum is passed, the number of boundaries removed in each increment is smaller and smaller and the slope decreases. Throughout the range of threshold angles the sample with the normal distribution had a higher inverse connectivity than the one with the bimodal distribution and was, therefore, less connected.

Analogous data for the Ni samples are shown in Fig. 7. The inverse connectivity exhibits the same general behavior of increasing in slope, moving through a maximum and then decreasing in slope. However, the curves are distinct from one another and from the SrTiO₃ results. These differences are connected to the presence of twins and the non-random misorientation distributions, which are discussed further below.

4. Discussion

Wanner et al. [27] presented results for the variation in B_0 and B_1 as a function of threshold angle for a microstructure with three different hypothetical misorientation distributions. The microstructure had a normal grain size

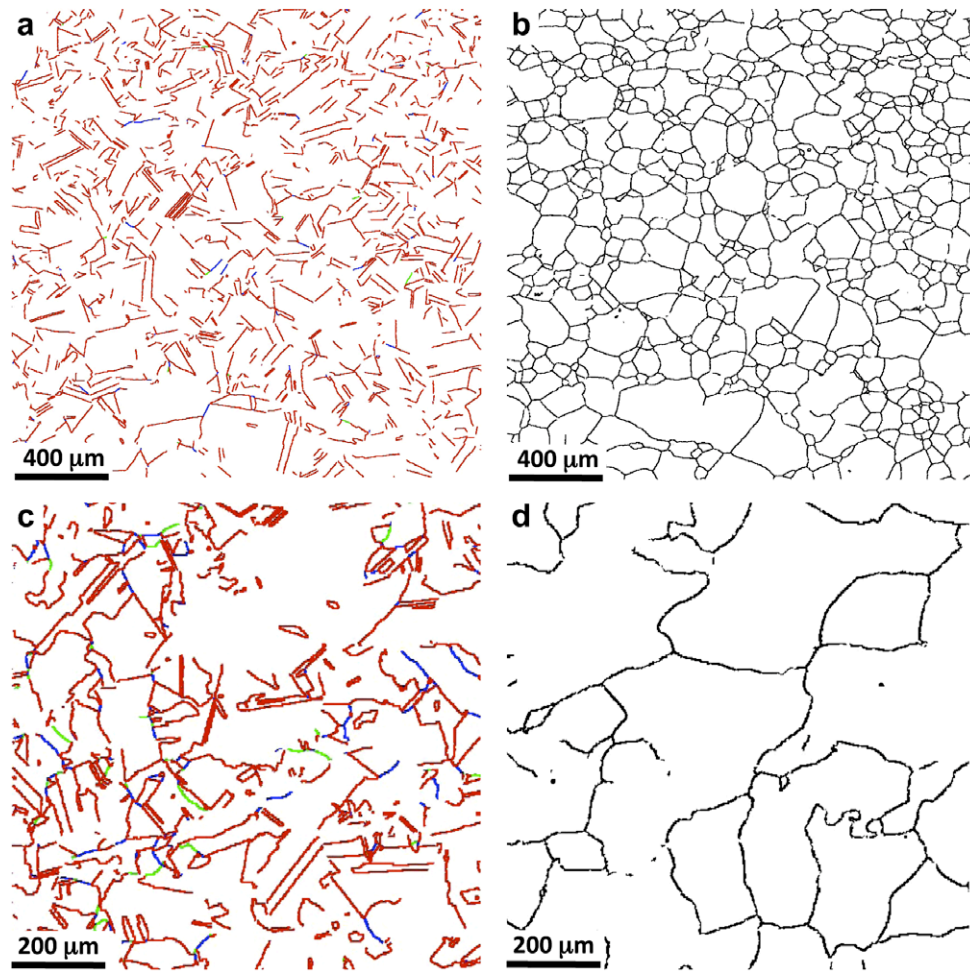


Fig. 5. Grain boundary maps for the Ni samples. (a) All of the $\Sigma 3'$ boundaries in low $\Sigma 3$ Ni, (b) all of the non- $\Sigma 3'$ boundaries in the low $\Sigma 3$ Ni, (c) all of $\Sigma 3'$ boundaries in high $\Sigma 3$ Ni, (d) All of the non- $\Sigma 3'$ boundaries in high $\Sigma 3$ Ni. In (a) and (c) the $\Sigma 3$ boundaries are colored red, the $\Sigma 9$ boundaries are blue and the $\Sigma 27$ boundaries are green. (For interpretation of the references to colour in this figure legend, the reader is referred to the web version of this article.)

distribution and about 800 grains and, while the ratio of B_0 – B_1 was not presented, the data allows us to infer that the ratio increased as a function of disorientation angle, in general agreement with what is reported here.

The increasing value of β_{01} with cut-off angle can be understood in the following way. If we begin by considering the ideal network, $B_0 = 1$ and B_1 is equal to the number of grains. For each boundary removed from the network two grains become one grain or, topologically, two closed paths become one closed path, and B_1 must decrease accordingly. B_1 will continue to decrease in proportion to the number of boundaries removed. As more boundaries are removed and the percolation threshold is approached disconnected fragments will be created and each additional fragment will increment B_0 , further increasing β_{01} . At this point boundaries can be removed to shrink the fragments without affecting B_1 . Therefore, the effect of removing boundaries on the decrease in B_1 will be smaller as there are fewer and fewer closed paths to disrupt. This causes β_{01} to increase at a smaller rate. The details of how β_{01} depends on the threshold angle depends upon relative grain

size and shape, how the grain boundaries are distributed with respect to misorientation angle and the way in which the grain boundaries are connected. Therefore, there is a microstructural signature in the curve of β_{01} vs. threshold angle that is apparent in the data presented in Figs. 6 and 7.

We begin by noting that β_{01} for the normal grain size distribution and the bimodal grain size distribution show only a small difference. The bimodal distribution shows a slightly lower ratio at all threshold angles, indicating that its relative connectivity is greater than that of the normal distribution. This is a signature of the larger grains. The larger grains have, on average, more sides than smaller grains. Boundaries removed from large grains are less likely to create a fragment than those removed from the matrix of smaller grains because of the continuous correlated path of boundaries around the large grains. These longer paths are evident in the images of boundaries remaining above 50° (see, for example, Fig. 6g). The dependence of inverse connectivity on the threshold angle is expected to be the same for all samples with an equiaxed

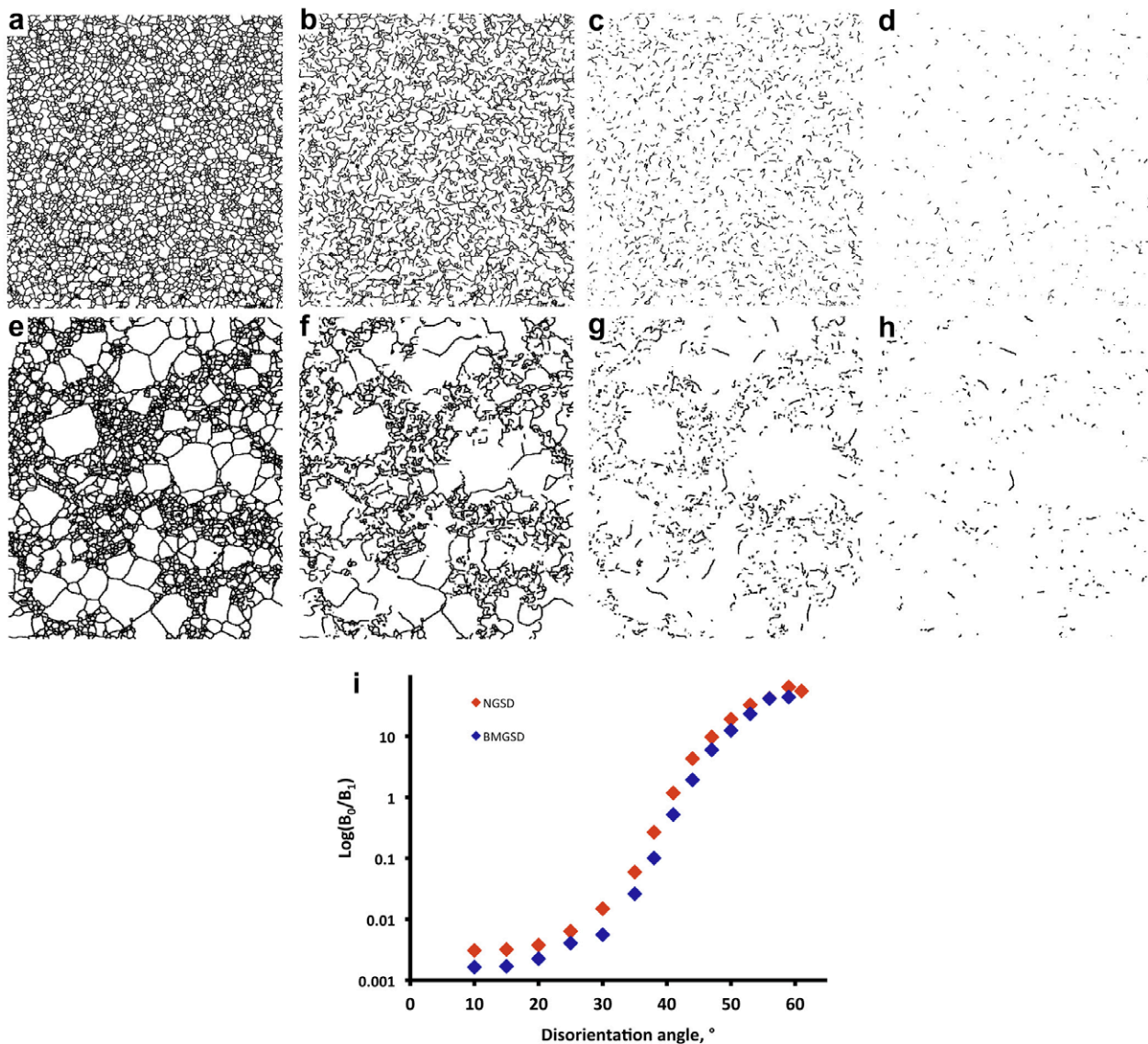


Fig. 6. Grain boundary networks for the SrTiO₃ samples as a function of disorientation threshold. (a–d) Thresholded boundary maps for bimodal SrTiO₃ for all boundaries with disorientation (a) >20°, (b) >41°, (c) >53° and (d) >59°. (e–h) Thresholded boundary maps for unimodal SrTiO₃ for all boundaries with disorientation (e) >20°, (f) >41°, (g) >53° and (h) >59°. (i) Plot of the inverse connectivity as a function of disorientation threshold for SrTiO₃ with a normal (NGSD) and bimodal (BMGSD) grain size distribution.

grain shape, a normal grain size distribution and a random misorientation distribution function.

Perhaps the most visually stunning result, quantified by the dramatic difference in β_{01} , is the difference between the $\Sigma 3''$ and non- $\Sigma 3''$ boundaries in the high $\Sigma 3$ and low $\Sigma 3$ samples (Fig. 5 and Table 1). In the low $\Sigma 3$ sample the $\Sigma 3''$ boundaries were highly disconnected ($\beta_{01} > 1$), while the non- $\Sigma 3''$ network almost looked like a normal microstructure and had a much smaller value of β_{01} . For the high $\Sigma 3$ sample the opposite was true. It was the $\Sigma 3''$ network that was highly connected and the non- $\Sigma 3''$ network that was disconnected. These same characteristics are illustrated in more detail in Fig. 7. The main difference in the variation in β_{01} with threshold angle was that the high $\Sigma 3$ sample had lower connectivity at low cut-off angles, due to a relative increase in B_0 due to the presence of island grains, and a

higher connectivity at higher cut-off angles, because there were more $\Sigma 3$ boundaries and they were more interconnected. The relatively disconnected nature of the random grain boundaries in Fig. 5d compared with Fig. 5b implies that the high $\Sigma 3$ microstructure would have greater corrosion resistance.

As mentioned earlier, the types of grain boundaries in the high and low $\Sigma 3$ samples have been characterized previously and three main differences were noted [6,28]. The first was that more of the grain boundary length in the high $\Sigma 3$ sample was $\Sigma 3$ type (63% compared with 42%). The second was that a large fraction of the $\Sigma 3$ boundaries were not on parallel (1 1 1) planes [we refer to any $\Sigma 3$ boundary not comprising two parallel (1 1 1) planes as “incoherent”]. In the high $\Sigma 3$ sample 44% of the $\Sigma 3$ boundaries were incoherent, while in the low $\Sigma 3$ boundaries 33% were incoherent.

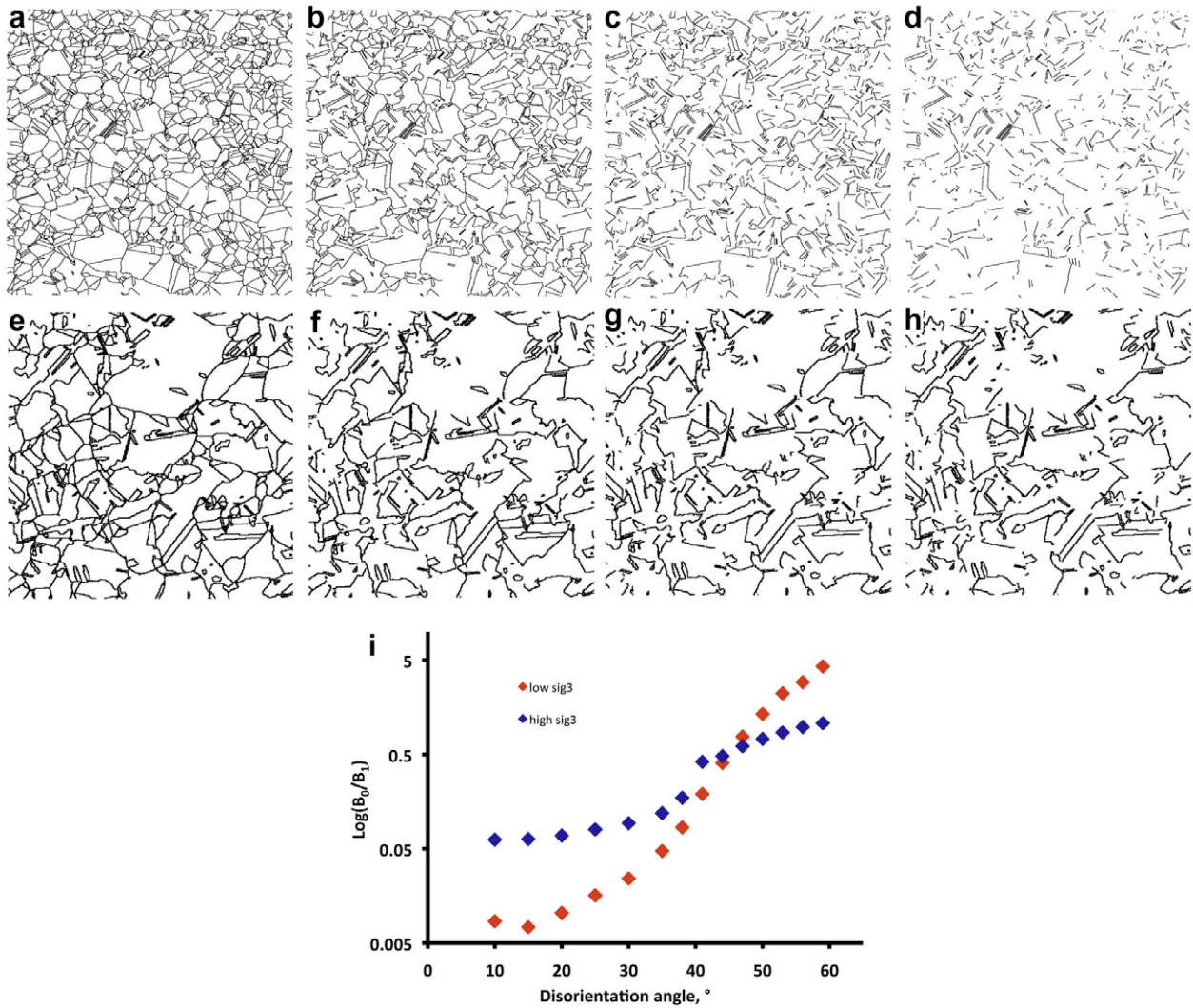


Fig. 7. Grain boundary networks for the Ni samples as a function disorientation threshold. (a–d) Thresholded boundary maps for low $\Sigma 3$ Ni for all boundaries with disorientation (a) $>20^\circ$, (b) $>41^\circ$, (c) $>53^\circ$ and (d) $>59^\circ$. (e–h) Thresholded boundary maps for high $\Sigma 3$ Ni for all boundaries with disorientation (e) $>20^\circ$, (f) $>41^\circ$, (g) $>53^\circ$ and (h) $>59^\circ$. (i) Plot of the inverse connectivity as a function of disorientation threshold for low and high $\Sigma 3$ Ni.

The third difference was that in the high $\Sigma 3$ sample a larger fraction of all of the triple junctions have at least two $\Sigma 3''$ boundaries that meet. In the high $\Sigma 3$ sample 49% of all triple junctions had at least two $\Sigma 3''$ boundaries, compared with 9% in the low $\Sigma 3$ sample [6]. Based simply on counting triple junctions, it is clear that there is a higher degree of correlation among the $\Sigma 3''$ boundaries in the high $\Sigma 3''$ sample, and this is reflected in the homology metrics.

This result reinforces a point brought out by Schuh et al. [19], that in extensively twinned microstructures the fraction of special boundaries is not a reliable indicator of the connectivity. Instead, it was found that triple junction content was an effective predictor of the largest clusters of random boundaries. This derives from the misorientation constraint at triple junctions, which demands that one of the grain boundaries that meets at a triple junction is always dependent upon the other two [33]. For example, if a $\Sigma 3$ and $\Sigma 9$ grain boundary meet, the third boundary must be $\Sigma 3$ or $\Sigma 27$. Therefore, as the concentration of

$\Sigma 3''$ grain boundaries increases there is a disproportionately larger probability that they will connect to similar boundaries, and this is reflected in the increased connectivity of the high $\Sigma 3''$ sample and the related decrease in connectivity of the random network.

Inverse connectivity appears to be a sensitive, scale independent measure that provides information that cannot be derived from knowledge only of the relative areas of grain boundaries. The results presented here indicate that it is sensitive to the grain size distribution, the presences of twins and the misorientation distribution. Future work will focus on extending the present calculations to three-dimensional microstructures, which are becoming more readily available [34–36]. For this extension it should be noted that there is an additional topological parameter for three-dimensional structures, B_2 , which is the number of enclosed cavities. This means that there may exist additional and analogous topological metrics for three-dimensional microstructures, such as the ratio of B_0 – B_2 . The investigation of

three-dimensional microstructures is of interest because features on plane sections that appear disconnected may actually be connected in the third dimension and, in addition to the well known misorientation constraint on grain boundaries at triple junctions, there is also a constraint on the grain boundary plane orientation that has not been fully explored. Specifically, all three grain boundary planes meeting at the triple line are constrained to lie in the same crystallographic zone. It is currently unclear if or how this will affect grain boundary character distributions.

5. Conclusions

The inverse connectivity β_{01} provides a measure of the degree to which a boundary network is connected. As β_{01} approaches zero the network is highly connected, approaching ideal. Increasing values of β_{01} indicate diminished connectivity. The inverse connectivity in twinned microstructures is greater than in untwinned microstructure; it is also larger in a sample with a normal grain size distribution compared with a sample with a bimodal grain size distribution. The variation in inverse connectivity with threshold disorientation is quantitatively different in two samples with different misorientation distributions. Specifically, the sample with more $\Sigma 3$ boundaries has greater connectivity within the $\Sigma 3''$ network and the network of random boundaries is less connected. The inverse connectivity provides information about the grain boundary network that cannot be derived solely from knowledge of relative grain boundary areas.

Acknowledgement

This work was primarily supported by the MRSEC program of the National Science Foundation under award number DMR-0520425.

References

- [1] Palumbo G, Lehockey EM, Lin P. *JOM* 1998;50:40.
- [2] Lin P, Palumbo G, Erb U, Aust KT. *Scripta Mater* 1995;33:1387.
- [3] Lehockey EM, Palumbo G, Lin P, Brennenstuhl AM. *Scripta Mater* 1997;36:1211.
- [4] Randle V. *Acta Mater* 2004;52:4067.
- [5] Rohrer GS, Randle V, Kim C-S, Hu Y. *Acta Mater* 2006;54:4389.
- [6] Randle V, Rohrer GS, Miller HM, Coleman M, Owen GT. *Acta Mater* 2008;56:2363.
- [7] Kim C-S, Rollett AD, Rohrer GS. *Scripta Mater* 2006;54:1005.
- [8] Rohrer GS, Saylor DM, El-Dasher BS, Adams BL, Rollett AD, Wynblatt P. *Z Metallkd* 2004;95:197.
- [9] Randle V. *Scripta Mater* 2006;54:1011.
- [10] Kumar M, King WE, Schwartz AJ. *Acta Mater* 2000;48:2081.
- [11] Frary M, Schuh CA. *Appl Phys Lett* 2003;83:3755.
- [12] Minich RW, Schuh CA, Kumar M. *Phys Rev B* 2002;66:052101.
- [13] Frary M, Schuh CA. *Phys Rev B* 2004;69:134115.
- [14] Frary M, Schuh CA. *Philos Mag* 2005;85:1123.
- [15] Frary M. *Scripta Mater* 2007;57:205.
- [16] Xia S, Zhou BX, Chen WJ, Wang WG. *Scripta Mater* 2006;54:2019.
- [17] Xia S, Zhou B, Chen W. *J Mater Sci* 2008;43:2990.
- [18] Reed BW, Kumar M, Minich RW, Rudd RE. *Acta Mater* 2008;56:3278.
- [19] Schuh CA, Kumar M, King WE. *Acta Mater* 2003;51:687.
- [20] Steele JH. Application of topological concepts in stereology. In: *Stereology and quantitative metallography*, ASTM STP 504. West Conshohocken (PA): American Society for Testing and Materials; 1972. p. 39–58.
- [21] Mecke KR. *Phys Rev E* 1996;53:4794.
- [22] Mecke Klaus R, Victor Sofonea. *Phys Rev E* 1997;56:R3761.
- [23] Mendoza R, Alkemper J, Voorhees PW. The topology of coarsened microstructures. In: Rappaz M, Beckermann C, Trivedi R, editors. *Solidification processes and microstructures: A symposium in honor of Wilfried Kurz*. Warrendale (PA): TMS; 2004. p. 123–9.
- [24] Mendoza R, Savin I, Thornton K, Voorhees PW. *Nat Mater* 2004;3:385.
- [25] Gameiro M, Mischaikow K, Wanner T. *Acta Mater* 2005;53:693.
- [26] Mendoza R, Thornton K, Savin I, Voorhees PW. *Acta Mater* 2006;54:743.
- [27] Wanner T, Fuller Jr ER, Saylor DM. *Acta Mater* 2010;58:102.
- [28] Miller HM, Kim C-S, Gruber J, Randle V, Rohrer GS. *Mater Sci Forum* 2007;558–559:641.
- [29] MacKenzie JK. *Biometrika* 1958;45:229.
- [30] Kaczynski TK, Mischaikow K, Mrozek M. *Applied mathematical sciences. Computational homology*, 157. New York: Springer-Verlag; 2004.
- [31] Kalies W, Pilarczyk P. *Computational homology program*; 2004. <<http://www.chomp.rutgers.edu/>>.
- [32] Brandon DG. *Acta Mater* 1966;14:1479.
- [33] Miyazawa K, Iwasaki Y, Ito K, Ishida Y. *Acta Cryst* 1996; A52: 787.
- [34] Groeber M, Ghosh S, Uchic MD, Dimiduk DM. *Acta Mater* 2009;56:1257.
- [35] Li J, Dillon SJ, Rohrer GS. *Acta Mater* 2009;57:4304.
- [36] Dillon SJ, Rohrer GS. *J Am Ceram Soc* 2009;92:1580.